

# A Cryogenic Neutron Radiometer for Absolute Neutron Fluence Measurement

Z. Chowdhuri<sup>a \*</sup>, G. Hansen<sup>a</sup>, W. M. Snow<sup>a</sup>, C. D. Keith<sup>a †</sup>, A. K. Thompson<sup>b</sup>, M. S. Dewey<sup>b</sup>, D. M. Gilliam<sup>b</sup>, J. S. Nico<sup>b</sup>, F. E. Wietfeldt<sup>b ‡</sup>, V. Jane<sup>a §</sup>, G. L. Greene<sup>b ¶</sup>

<sup>a</sup>Indiana University Cyclotron Facility, Bloomington, IN 47408

<sup>b</sup>National Institute of Standards and Technology, Gaithersburg, MD 20899

We describe the measurement principle, design, operation, measurements of noise and linearity of response, and evaluation of systematic effects for an electrical substitution radiometer which measures the absolute neutron fluence of thermal neutron beams based on neutron absorption in a <sup>6</sup>Li-rich metallic alloy. We demonstrate that the device possesses a linear response to electrical power in the 50-500 nW range with better than 0.1% absolute accuracy and negligible zero offset. We show the response of the radiometer to power delivered by a 3 meV neutron beam. We compare the noise of the radiometer to the noise observed upstream in a thin fluence monitor and show that the radiometer noise is understood quantitatively. We establish that the radiometer measures neutron fluences above 10<sup>5</sup> n/s to an absolute accuracy of 0.1%.

## 1. Introduction

### 1.1. Motivation

Precise knowledge of the decay rate of the neutron is important for weak interaction theory (determination of the KM matrix element  $V_{ud}$  and tests of weak interaction universality) [1] and for predictions of the primordial fraction of <sup>4</sup>He in the universe according to the Big Bang theory [2]. One important method of measuring the neutron lifetime relies on a measurement of both the absolute rate of production of decay products in a section of a neutron beam and the absolute density of neutrons in the beam. With the development of the Penning trap technique for trapping and counting the protons for in-beam neutron decay

[3], absolute measurement of the neutron density has become the limiting factor in neutron decay rate measurements using beams.

With the possible exception of a device using neutron absorption in <sup>10</sup>B [4], there have been no absolute neutron fluence measurements based on the usual counting methods, either performed or proposed, which are capable of reaching the absolute accuracy of 0.1% required for neutron lifetime measurements. It is this problem which motivated the original proposal [5] and the further development [6–8] of radiometric methods for absolute neutron fluence measurement.

In addition to its application to in-beam neutron lifetime measurements, advances in absolute neutron flux measurement can also be used to improve the precision of neutron fluence standards.

### 1.2. Electronic Substitution Radiometry for Neutron Beams

The essence of the idea behind electronic substitution radiometry (ESR) is applicable in principle to any particle beam and in practice has been used to measure fluences of almost everything [9–20]. Electronic substitution radiometers measure the power deposited by some fluence of radiation in a totally-absorbing target through

\*Present address: National Institute of Standards and Technology, MD 20899 and Department of Materials and Nuclear Engineering, University of Maryland, College Park, MD 20742

†Present address: Thomas Jefferson National Accelerator Facility, Newport News, VA 23606

‡Present address: Physics Department, Tulane University, New Orleans, LA 70118

§Present address: Physics Department, Michigan State University, East Lansing, MI 48824

¶Present address: Physics Department, University of Tennessee, Knoxville, TN 68527 and Physics Division, Oak Ridge National Lab, Oak Ridge, TN 37831

comparison to an equivalent amount of electrical power [21]. The technique consists of the following steps: (1) The beam is totally absorbed in a target. (2) The energy of these interactions is also totally absorbed inside the target. (3) All of this energy contributes to the thermal power delivered to the target. (4) The absolute power delivered to the target is measured by an appropriate substitution of electrical power from a heater. (5) This power divided by the energy per interaction of the particle beam (assumed to be known independently) measures the fluence of the beam, which is defined as the absolute number of beam particles per second striking the target.

The practical limits to the accuracy of ESR for thermal neutrons depend on the degree to which the idealized steps outlined above can be realized for real neutron beams and absorbers. The remainder of this paper is a description of precisely these limits in our device.

## 2. The Neutron Radiometer

In an ESR a beam of particles is directed at a target equipped with an electrical heater and optimized for absorption of the beam. The radiometer is operated as a dual-compensated device in which the temperature at each end of a weak thermal link (Fig. 1) is actively controlled to maintain a constant temperature gradient, and therefore constant heat flow, across the link. If the thermal conductance of the link is  $k$ , the heat flow for a small temperature gradient is

$$\dot{Q} = k\Delta T. \quad (1)$$

The heat that flows from the target to the heat bath is the sum of two contributions: one from the absorbed beam and the other from the electrical heater. When the beam is closed by a shutter, the electrical power to the target must be increased to maintain the target temperature, and hence the temperature difference between that and the heat bath. This electrical power to the target,  $P$  is measured in both cases, and the difference yields the power delivered by the beam:

$$P_{\text{beam}} = P_{\text{beam off}} - P_{\text{beam on}}. \quad (2)$$

In the case of the neutron radiometer, the incident neutrons are completely absorbed in an

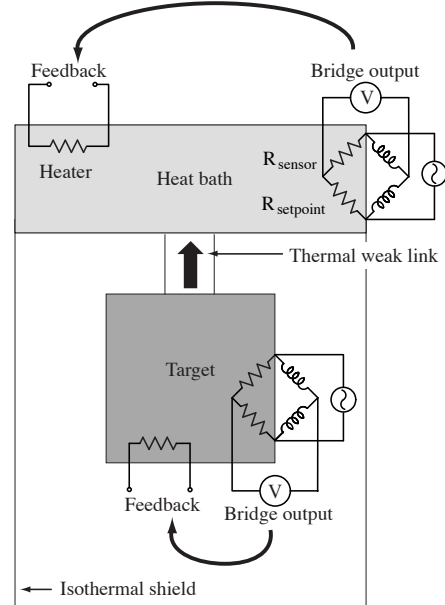


Figure 1. Radiometer measurement technique

exothermic nuclear reaction of known energy,  $Q_{\text{reaction}}$ . The charged species that are produced in the reaction carry this energy and as they thermalize in the target their kinetic energy is converted to heat in the bulk material. If all of the energy generated in the neutron absorption reaction is thermalized and appears as heat in the target, then the neutron fluence is:

$$\Phi = \frac{P_{\text{beam}}}{Q_{\text{reaction}}}. \quad (3)$$

Given the size of typical neutron fluences, it is clear that any such device must be operated at low temperatures. Consider the order of magnitude of the power that a thermal neutron beam can deliver to a totally-absorbing object. The energy released in a neutron-induced nuclear reaction (a few MeV per neutron, neglecting fission for the moment) is much larger than the kinetic energy of a thermal neutron (about 25 meV), so all the energy comes from the nuclear reaction. A neutron fluence of order  $10^6$  neutrons per sec-

ond striking the target then delivers about a microwatt of power. The heat capacities of solids at room temperature are much too large to resolve the resulting temperature changes on a realistic time scale. One must resort to low temperatures to lower the heat capacity. Another means of minimizing the heat capacity is by decreasing the size of the absorber: this favors the use of a material with large neutron absorption cross section.

### 2.1. The Neutron Absorber

There are several considerations in choosing a target material for a neutron radiometer. Since the measurement relies on full absorption of the energy released in the nuclear reaction induced by the neutrons, it is imperative to select an isotope which has one primary reaction channel with well known Q-value and reaction products that cannot escape the target. Nuclei which produce gammas (or fast neutrons produced in fission) upon neutron capture are unacceptable because the mean free path of MeV gammas in typical materials is large compared to the neutron absorption length. This condition alone eliminates almost all nuclei from consideration. Robertson [5] suggested two possible targets,  $^3\text{He}$  and  $^6\text{Li}$ , with the properties listed in Table 1. Both of the neutron reactions in these nuclei possess a dominant reaction channel that produces charged particles in the few MeV range, which have short ranges in matter and are easily stopped in the target. In both cases, the reaction products are created in their ground states, so there is no loss of energy from gamma emission. Although  $^3\text{H}$  is unstable, its beta decay possesses both a long half-life (12.3 years) and a small energy release (18.6 keV) which deposits a very small fraction of the total power to the target.

As can be seen in the table, a  $^3\text{He}$  target has the severe disadvantage relative to  $^6\text{Li}$  of lower energy release from the reaction by almost a factor of 7. In addition,  $^3\text{He}$  possesses a higher heat capacity per neutron absorption length than  $^6\text{Li}$  for most temperatures, since it remains a liquid at low temperatures under its own saturated vapor pressure. The high heat capacity lengthens the thermal time constant, thereby lowering the usable on-off beam chopping frequency and in-

creasing the signal-to-noise ratio. We have therefore chosen to develop a radiometer based on a  $^6\text{Li}$ -rich target. It is mainly the properties of  $^6\text{Li}$  which limit the accuracy of the method.

	$^3\text{He}$	$^6\text{Li}$
Reaction	$^3\text{He}(n,p)^3\text{H}$	$^6\text{Li}(n,^4\text{He})^3\text{H}$
$\sigma_0$ (b)	5319.3(15.9)	941.7(2.8)
Q-value (MeV)	0.763763(4)	4.78293(47)
Power (nW)	36.7108(2)	229.89(2)

Table 1

Nuclei suitable for use as a neutron radiometer target. Cross section data from ENDF/B-VI at <http://t2.lanl.gov/cgi-bin/nuclides/endf> and Q-values from the NuBase database at <http://nucldata.nuclear.lu.se/database/masses/> utilizing the Audi-Wapstra mass tables. The power is calculated for a beam with a fluence of  $3 \times 10^5 \text{ n s}^{-1}$ .

The properties of  $^6\text{Li}$  which are important for absolute radiometry are as follows. The energy release of the  $^6\text{Li}(n,^4\text{He})^3\text{H}$  reaction is 4.78293(47) MeV: the 0.01% accuracy sets an upper limit to the accuracy of the radiometer. The cross section of the  $^6\text{Li}(n,^4\text{He})^3\text{H}$  reaction for 25 meV neutrons is 941(3) barns. This is very large compared with (a) the  $^6\text{Li}(n,\gamma)^7\text{Li}$  reaction cross section which is 0.039(3) barns, (b) the typical size of the  $(n,\gamma)$  cross sections for other nuclei (1-2 barns), including likely contaminants ( $^7\text{Li}(n,\gamma)^8\text{Li}$  has a 0.045(3) barn cross section), and (c) the total scattering cross section for neutrons on  $^6\text{Li}$  (0.75(2) barns) and other materials (a few barns). Thus an isotopically pure  $^6\text{Li}$  target is not required:  $^6\text{Li}$ -enriched material will suffice.

Natural lithium contains 7.59 at.%  $^6\text{Li}$ ; the rest is  $^7\text{Li}$ . The targets used in this work were made with lithium enriched to 94% in  $^6\text{Li}$ . A pure solid lithium target is unacceptable because of a martensitic phase transformation at 80 K from a body-centered cubic (BCC) structure to a mixture of different structures whose exact nature

remains controversial [22–29]. This phase transition can introduce a time-dependent heat evolution from the target. In order to eliminate this possibility, it is necessary to add in a transformation inhibitor chosen for minimal interaction with neutrons.

There is another important constraint for a solid radiometer target: it must be metallic. Absolute radiometers must thermalize the reaction products to high accuracy. Since the target is solid it is susceptible to radiation damage, and the energies of the reaction products in  ${}^6\text{Li}$  are large enough to create some lattice vacancies and interstitials in the polycrystalline target. The free electron gas in a metal plays an important role in reducing the number of metastable modes for energy storage in the solid relative to an insulator. Radiation damage questions, which are at the  $10^{-3}$  level, are discussed in more detail in section 5.7.

A lithium-magnesium alloy fits all these constraints.  ${}^6\text{LiMg}$  alloys of less than 74 at.% do not possess the solid-solid phase transition [30]. Magnesium has a small neutron scattering and absorption cross section. The sample of  ${}^6\text{Li}_{0.74}\text{Mg}_{0.26}$  used in our radiometer was made at the Indiana University Cyclotron Facility [31]. The alloy was formed in an RF induction furnace and annealed at 480 K to minimize pre-existing interstitials and vacancies in the alloy matrix. The target contains 2.45 grams of 73.8 at.%  ${}^6\text{Li}$  and is in the form of a disk 0.28 cm thick and 3.79 cm in diameter. It was press-fit into a 48-gram aluminum cell and sealed under argon. A thin coating of Apiezon grease was applied to the back of the disk to provide improved thermal contact to the case.

The attenuation length for 5 meV neutrons in  ${}^6\text{Li}$  is about 0.013 cm, so the neutron transmission through the 0.28 cm thick target is completely negligible. The thin aluminum cover of the cell serves to capture any of the recoiling charged reaction products that might otherwise escape. The range of a 2.7 MeV  ${}^3\text{H}$  in aluminum is 0.0064 cm and for the  $\alpha$  particle it is smaller still, thus a thin sheet is all that is required to absorb them. The presence of the aluminum requires a small correction to the fluence measurement because it

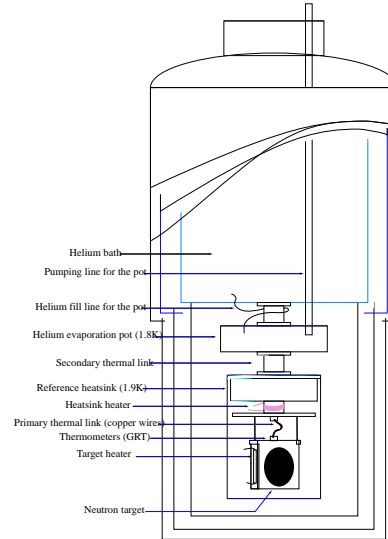


Figure 2. The neutron radiometer

attenuates the neutron beam.

## 2.2. The Radiometer Cryostat and Thermal Isolation

The neutron radiometer shown in Fig. 2 is based on an Oxford Instruments MD25 cryostat with a central liquid  ${}^4\text{He}$  can with a 25 l capacity. Surrounding this is a 45 l annular liquid nitrogen reservoir. The nine-day hold time for liquid helium in this cryostat during refrigerator operation was sufficient for the maintenance of stable measurement conditions. The vendor-supplied cryostat was modified to operate below 4.2 K by incorporating an evaporation pot. The temperature and cooling power of the pot is coarsely controlled by regulating the vapor pressure over the liquid helium in it by means of a vacuum regulator valve from Lakeshore Cryotronics, Inc. The vapor pressure was maintained around 17 mbar which corresponds to a temperature of 2 K. This is below the superfluid transition temperature, so the temperature of the liquid in the pot (and therefore the pot as a whole, since the liquid dominates the heat capacity) is isothermal to an excellent

approximation. Thermal gradients in the superfluid lead to bulk superfluid flow which quickly equalizes the temperature. This helps to stabilize the temperature of the pot and filter out thermal noise from room temperature to the isolated heat bath and target stages.

There are four radiation shields in the cryostat: a room temperature shield which is the vacuum can, a 77 K shield attached to the liquid nitrogen reservoir, a 4 K shield which is bolted to the liquid helium bath, and finally, a temperature controlled shield anchored to the heat bath. In order to reduce the neutron fluence losses in the shields, there are windows made of  $9 \times 10^{-4}$  cm thick aluminum foil. This is still thick enough to absorb the IR radiation emitted from successive thermal radiation shields. However, the neutron attenuation in these windows must be accounted for (section 5.3).

In our device, the thermal link between the target and the heat bath is a bundle of 34 oxygen-free high-conductivity copper wires, each 0.09 mm in diameter and 38 mm in length. The conductance of the bundle is  $8.3 \times 10^{-4}$  W K<sup>-1</sup> at 2 K. The mechanical support for the target is provided by two threaded polyamide (DuPont Vespel 22) posts. This material has very low thermal conductivity (at 2 K,  $\kappa = 2 \times 10^{-5}$  W cm<sup>-1</sup> K<sup>-1</sup>) and the combined conductance for the two posts is  $1.2 \times 10^{-6}$  W K<sup>-1</sup>, more than two orders of magnitude smaller than that of the copper wires. In addition to the loss of heat from the target through the support rods, there is also conduction through the lead wires and the residual gas, as well as radiative losses. Apart from these latter two mechanisms, all conduction paths lead to the heat bath. The corrections to the measurement due to these alternate heat conduction paths are estimated in section 5.5.

### 3. Electrical Power Measurement Technique

The ESR measurement technique requires the temperatures of the target and heat bath to be held constant so that the heat flow between them is constant. Since the beam is chopped, and the difference between the feedback power in the two

states of the beam is used to determine the input power, the absolute values of the temperatures are unimportant. What is important is that they be constant and the temperature noise sets a limit to the accuracy of the measurement. To measure 1  $\mu$ W of power flowing through a thermal conductance of  $10^{-3}$  W K<sup>-1</sup> to nW precision requires  $\mu$ K local temperature stability of the target and heat bath.

There are two separate temperature control circuits for the heat bath and the target. A schematic of the electronics is given in Fig. 3.

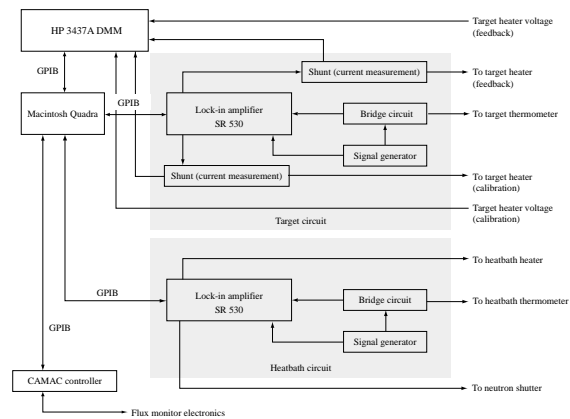


Figure 3. Block diagram of the radiometer electronics.

The temperature sensors used in this measurement are lithium-doped germanium resistance thermometers (GRT) with typical sensitivity of  $dR/dT = 1000 \Omega \text{ K}^{-1}$  near 2 K. They are included as arms of Wheatstone bridge circuits where their resistance can be compared very accurately to that of a constant precision resistor. This precision metal foil resistor is chosen to be close to the value of the GRT resistance at the operating temperature. The other two legs of the bridge consist of a six-decade ratio transformer. The ratio transformer increases the stability of the bridge setpoint (inductive voltage division is

typically more stable than resistive division since it depends on geometry as opposed to materials properties) and also provides the option of changing the setpoint easily with an adjustment performed at room temperature.

There is stray capacitance in the lead wires which gives rise to an out-of-phase signal on the bridge output. This capacitance varies slowly with time due to changing cryogen levels. A variable capacitor is incorporated into the circuit to zero it manually. Typically this must be done once a day.

The control system operates by monitoring the error signals from the bridges and generating appropriate feedback powers to the heat bath and target to drive the error signals, and therefore the temperature differences, to zero. The bridges are driven with sinusoidal voltages and the error signals are read by two Stanford Research Systems SR530 lock-in amplifiers. Incommensurate frequencies (748 Hz and 919 Hz) were chosen to suppress possible electronic cross-talk. Both frequencies were used interchangeably on the heat bath and the target bridges with no discernable systematic difference in measured power.

The RMS output of the bridge is

$$V_0 = V_i \left( \alpha - \frac{R_S}{R_T + R_S} \right) \quad (4)$$

where  $V_i$  is the input RMS voltage,  $R_S$  is the setpoint resistance,  $R_T$  is the resistance of the thermometer, and  $\alpha = L_1/(L_1 + L_2)$  is the inductance ratio set by the ratio transformer. The input voltage,  $V_i$ , is chosen to be as large as possible without causing too great a power dissipation in the thermometers. In normal operation, this excitation voltage was 15 mV for the heat bath and 8 mV for the target. The resulting power dissipated in the target by this excitation is about 8 nW. As long as this is constant, it contributes equally to the beam-on and beam-off power measurements, and taking the difference between the two removes the offset. The stability of the amplitude of the excitation voltage was measured to be better than 1 in  $10^4$ , thus the fluctuations of this offset are at the pW level and therefore negligible.

The lock-in amplifiers read the output signals

from the bridge circuits and the information is collected by the system software to be used in the digital PID loops for temperature control. Each lock-in has two programmable voltage outputs and these are used to generate the feedback voltages for the temperature control heaters.

The voltages that are used to calculate the feedback power are read by a Hewlett-Packard 3437A digital multimeter. The absolute accuracy of each measurement is  $15 \mu\text{V}$  on the 3 V scale, and is limited by the integration time of 1.7 ms. Hundreds of readings are averaged together for each voltage recorded by the DAQ, so the contribution to the error from the multimeter is negligible.

The feedback signal is calculated in software based on the magnitude and time dependence of the bridge signals. The usual proportional-integral-differential (PID) algorithm is used with an additional high frequency filter, a preamplifier, a post-PID amplifier, and a final linearization stage. Since the change in the bridge signal is directly proportional to feedback power and power is proportional to  $V^2$ , a square root operation is incorporated into the feedback algorithm. We use the Ziegler-Nichols [32] closed-loop method to determine the optimum settings for the PID gains in the control algorithm.

With the thermometers, a typical error signal on the bridge of  $1 \text{ nV Hz}^{-\frac{1}{2}}$  corresponds to a temperature noise of about  $100 \text{ nK Hz}^{-\frac{1}{2}}$ .

#### 4. Offline Tests and Calibration

Extensive tests were performed on the radiometer to study its response to the addition of power to the target and to characterize systematic effects. There are several heaters on the target, attached at different locations on the back and the sides. One of the heaters is used to control the temperature of the target, and any one of the remaining heaters can be used to add a known amount of electrical power. The feedback and the test input powers are measured independently. Since the thermal conductivity of the target is larger than that of the weak link by about 3 orders of magnitude, we expect (and observe) no dependence of the measured power on the spatial location of the test input power.

The measurement of the power involves the measurement of the current,  $I$ , through the resistor, and the voltage  $V$  across it. The current is determined by measuring the voltage across a precision shunt resistor. The value of the heater resistance (20 k $\Omega$ , with 0.01% tolerance and measured to 1 ppm) is chosen to be large compared to the lead resistances so that the power dissipated in the leads is negligible (less than  $10^{-4}$  of the power dissipated in the heater). Thermoelectric effects associated with thermal gradients are suppressed in our measurement since the temperatures of the two ends of the thermometer are equal to high accuracy. Current-dependent thermoelectric effects (e.g. the Seebeck effect) change sign with the direction of current flow. The typical size of such effects for the materials that compose our thermometers and wires are in the microvolt range and are small compared to the voltages we measure. We switched the direction of the current in some of the calibration runs and found no difference in the measured values at the  $10^{-4}$  level.

In the tests, a known amount of power is added in cycles by chopping the input voltage on and off. There is an equilibration time associated with the feedback response to the change in the input power that must be considered in choosing the period of the chopping cycle. The time constant is a function of the target and weak link properties and is given by:

$$\tau = \frac{c}{\kappa}, \quad (5)$$

where  $c$  is the heat capacity of the target and  $\kappa$  is the thermal conductance of the weak link. Figure 4 shows a measurement which determines the open-loop time constant of the target. The time constant with a conductance of  $2 \times 10^{-4}$  W K $^{-1}$  is about 90 seconds, implying a heat capacity of about  $2 \times 10^{-2}$  J K $^{-1}$ . In the data analysis, the points corresponding to the first two minutes in a half-cycle are therefore discarded. We saw no systematic change in the measured power as a function of the fraction of data cut from the beginning of a cycle beyond the first two minutes.

Figure 5 illustrates the response of the instrument to electrical power added via a second

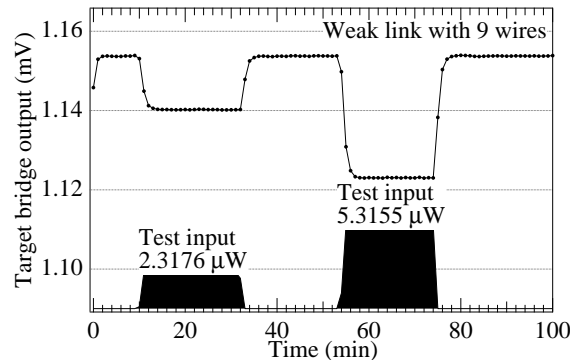


Figure 4. Change in the target bridge open-loop error signal with a change in input power.

heater on the target. The control program was set to generate random voltages with a 40 minute period covering a range that encloses the power anticipated from the neutron beam. Results from calibration runs are given in Fig. 6, where the power sensed by the radiometer is plotted against the electrical test input power. A straight-line fit to the data yields the following dependence of the sensed power on the input power (in nW):

$$P_{\text{sensed}} = 0.003(27) + 1.000000(85)P_{\text{input}}. \quad (6)$$

The response of the radiometer is thus linear within  $\pm 0.008\%$  of the input power. The power measured by the radiometer extrapolates to zero at zero input power within  $\pm 0.03$  nW. For a 300 nW input, this corresponds to an uncertainty of 0.01%. The success of this extrapolation to zero input power demonstrates the absence of an entire class of possible measurement errors which take the form of an addition to the measured power. However, it does not eliminate systematic errors which scale linearly with the added power. This latter class of systematic errors is discussed in the next section.

These measurements also address some aspects of the fundamental question of the equivalence of beam power and electrical power. One of the possible sources for a difference between the two is a difference in the pattern of heat flow generated by

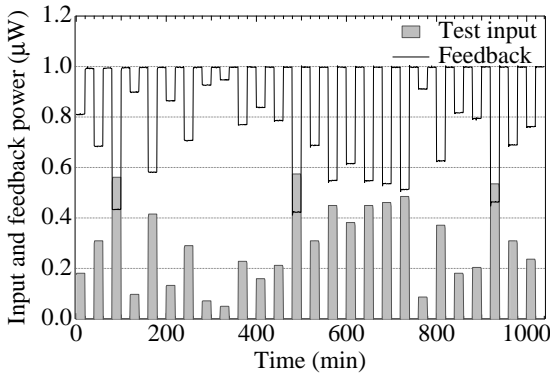


Figure 5. Testing the radiometer with different input powers in Run 96F031. The upper trace shows the feedback power for the radiometer and the lower trace (shaded) is the random input power.

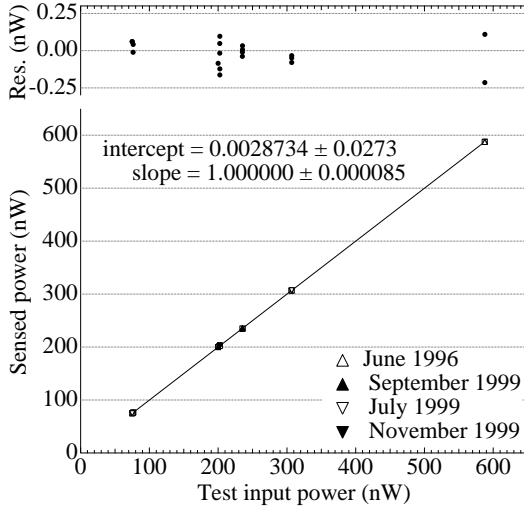


Figure 6. Power sensed by the radiometer for different test inputs. The error bars are much smaller than the symbols.

the neutron beam and the electrical heater. From detailed analyses of the thermal response of cryogenic radiometers for light [33], it is known that such differences are minimized if (1) the thermal resistances inside the target are small compared to the thermal resistance of the weak link, and (2) if the thermometer for the target is placed next to the contact between the thermal weak link and the target (this eliminates effects of thermal gradients). In the limit where the thermal weak link is the only path for heat conduction away from the target and the thermometer is placed exactly at the weak link joint (as in our case), the measured powers are the same in steady state due to conservation of energy even with different thermal resistances for the two paths. Based on a simple thermal model of the target given the known thermal conductance of the weak link, support posts, aluminum sample holder,  ${}^6\text{LiMg}$  target, and thermal boundary resistances, and the position of the thermometers, we estimate that the difference between registered power from a heater anchored to the aluminum case of the target and from the neutrons in the  ${}^6\text{LiMg}$  alloy is less than  $10^{-4}$ .

The measured data is consistent with this estimate. Although it was impractical in our case to distribute the electrical power directly into the  ${}^6\text{LiMg}$  through the indium vacuum seal on the target cell, we could direct the power into external heaters connected to the aluminum case with different thermal resistances between the thermometers and the case. The data in Fig. 6 includes runs in which the resistors used as the feedback and input heaters were swapped to test if the response has a spatial dependence. The results of the measurements indicate that no such location-specific systematic effects exist. This means that there are no loss mechanisms that vary according to the external location of power deposition in the target.

## 5. Systematic Corrections in the Radiometer

In order to make an absolute measurement, it is imperative to quantify all the loss mechanisms and apply them as corrections to the rate measured by the radiometer. A detailed discussion of

	$\alpha$	proton
Charge ( $\mu\text{C}$ )	90.54	92.98
Number (N)	$2.83 \times 10^{14}$	$5.80 \times 10^{14}$
Beam energy (J)	93.9	252.3
Energy lost (J)	$5.56 \times 10^{-7}$	$3.37 \times 10^{-6}$

Table 2

Results from PIXE measurements on  ${}^6\text{LiPb}$ . The beam energy shown in the third row is that delivered to the target by N projectiles and the last row in the table lists the total energy represented by the PIXE spectrum. As expected, the fraction of energy lost to x-rays escaping the front face of the target is completely negligible.

the systematic corrections is presented here. At this point, we emphasize that the size of all systematic corrections is below 1% and that therefore 5% accuracy is required of the auxiliary measurements and calculations performed to determine these corrections given our 0.1% absolute accuracy goal.

### 5.1. Production of x- and $\gamma$ - Rays in the Radiometer Target

Two different auxiliary measurements were performed to measure x rays and  $\gamma$  rays produced in the target: (1) particle-induced x ray emission (PIXE) for x rays up to 30 keV, and (2) prompt gamma activation analysis (PGAA) for photons with energy up to 10 MeV.

PIXE measures the prompt x rays induced by the impact of MeV charged particle beams. Since the cover on the  ${}^6\text{LiMg}$  target (necessary to protect the material against oxidation in air) would prevent the ions from reaching the target, the PIXE measurements were performed instead on an inert  ${}^6\text{LiPb}$  target.

The products of the  $n + {}^6\text{Li}$  reaction are a 2.071 MeV  $\alpha$  particle and a 2.715 MeV triton. In the measurement, the effect of the tritons was simulated using 0.9 MeV protons to reproduce the same energy per nucleon. In table 2, the energy in the third row is that delivered to the target by N projectiles. The last row is the energy represented by the PIXE data: less than a part in  $10^7$  is lost

via this channel. Thus, we can safely ignore x rays as a source of systematic error. This assumption may be extended to  ${}^6\text{LiMg}$  based on the knowledge of the constituents of that target and their expected interactions with the  $\alpha$  particles and the tritons. These results are also in agreement with TRIM calculations (see section 5.7) of the particle and photon transport. The physical reasons why the loss of energy due to x rays is so small are (1) the low Z of the target nuclei, leading to smaller x ray energies, and (2) the efficient transfer of energy by the Auger effect, which causes the fluorescence yield to be much smaller than one for K and L shells in light elements.

For higher photon energies we employed the prompt gamma activation analysis technique. The detector in the PGAA facility is a GEM series HPGe crystal with an active energy range from 100 keV to 10 MeV. Since secondary nuclear reactions in the target are likely to produce  $\gamma$ - rays, this measurement also serves to set a limit on the power deposited in the target by them. Finally, the measurement also doubled as an assay of the target composition which ensured that no significant amount of neutron-absorbing impurities were present.

The results from the PGAA analysis for the  ${}^6\text{LiMg}$  target and the background spectrum are given in Fig. 7. Based on this data we can calculate the heating in the target due to absorption of the  $\gamma$ - rays. For the low Z materials that compose this target this effect is less than 1 in  $10^6$  of the heat delivered by the neutron beam.

The energies of the  $\gamma$ - rays identify the constituents of the target. The  $\gamma$ - lines from  ${}^{28}\text{Si}$  and  ${}^{71}\text{Ge}$  are background from the PGAA instrument. The  $\gamma$ - lines from neutron absorption in the  ${}^{27}\text{Al}$  cover are clearly visible and all other expected components are seen. PGAA also serves as a method to assay the composition of the target with a weighting proportional to the neutron absorption cross sections of any impurities. The level of impurities in the  ${}^6\text{LiMg}$  itself as seen by PGAA is negligible.

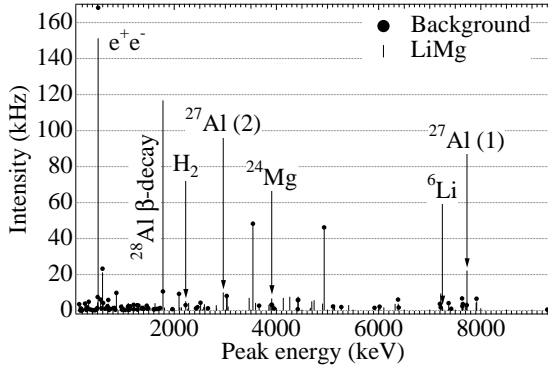


Figure 7. Neutron rates in the peaks of the  ${}^6\text{LiMg}$  PGAA spectrum. The solid dots are background on the PGAA instrument and the vertical lines are the signal with the  ${}^6\text{LiMg}$  target in place.

## 5.2. Secondary Nuclear Reactions in the Radiometer Targets

In principle, it is possible for the  $n + {}^6\text{Li}$  reaction products to undergo secondary nuclear reactions with the target nuclei and create fast neutrons,  $\gamma$ -rays or electrons from beta decay which change the energy deposited in the target. Our approach to the evaluation of this systematic effect is to calculate it using the extensive database on low energy nuclear reactions. The PGAA work gives us information on the materials present in the target and we have done an extensive search on all possible nuclear reactions given the target constituents and the energies of the  $\alpha$  particles and the tritons. Table 3 lists those reactions which could modify the deposited power in the target. The list is relatively short because the energies of the triton and  $\alpha$  particle from the neutron absorption reaction are below threshold for most of the possible nuclear reactions with the target nuclei, due in part to the Coulomb barrier. The net result is a small loss of energy from the target of 0.05%.

## 5.3. Neutron Attenuation in the Radiation Shields and Target Cover

The neutron beam passes through three radiation shields after the fluence monitor, but before the radiometer target. Thus, there is a correction associated with the absorption and scattering of the neutrons by the shield material that must be added to the neutron rate reported by the radiometer to obtain the fluence entering the device. The effect is minimized by fitting the shields with thin aluminum windows in the path of the beam. The windows need only be thick enough to absorb visible and IR radiation. Each window is 0.001 cm thick, for a total thickness of 0.003 cm. The total cross section of the aluminum alloy (6061-T6) used for the windows and the cover was measured to be 0.74 b at 3.3 meV. This neutron energy falls near the minimum of the total neutron cross section on aluminum because it is just below the Bragg cutoff for diffraction in aluminum. The combined attenuation ( $\sigma_{\text{abs}} = 0.24$  b,  $\sigma_{\text{scatt}} = 0.50$  b) is therefore 0.015% of the incident beam. A small part of these scattered neutrons which travel near the forward direction are also captured by the target. Only the closest radiation window at 2 K presents a non-negligible (1 steradian) solid angle to the target. The correction due to this effect is below  $10^{-5}$ . As a result, all the neutrons scattered by the windows are considered to be lost from the radiometer.

In addition to the absorption and scattering in the windows, there is also attenuation in the target cover. In this case, the absorption and the scattering must be considered separately since only half of the incoherent scattering results in a loss of neutrons from the target. As the energy of the neutrons is below the Bragg cutoff for aluminum, the scattering is isotropic to a good approximation and half the scattered neutrons are produced in the forward direction which are subsequently absorbed in the target. For the 0.013 cm thickness in the cover, the total attenuation is  $(0.07 \pm 0.01)\%$ . Multiple scattering of the neutrons is negligible.

Reaction	Q-value (MeV)	Incident particle energy (MeV)	Cross section	Comments
${}^6\text{Li}(n,\alpha){}^3\text{H}$	4.7829	25.0 meV	941 b	Primary channel
${}^6\text{Li}(t,p){}^8\text{Li}$	0.80	2.72	32.2 mb	Fraction lost: $3 \times 10^{-5}$
${}^6\text{Li}(n,\gamma)$	7.25	25.0 meV	38.5 mb	Fraction lost: $3.2 \times 10^{-4}$
${}^6\text{Li}(t,n){}^8\text{Be}$	16.02	2.04	$33.2 \text{ mb sr}^{-1}$	Fraction lost: $1.5 \times 10^{-4}$
			Contribution from the secondary ${}^6\text{Li}$ reactions (loss): $5.0 \times 10^{-4}$	
${}^7\text{Li}(t,\alpha){}^6\text{He}$	9.84	2.86	7.31 mb	Fraction gained: $3 \times 10^{-8}$
${}^7\text{Li}(n,\gamma){}^8\text{Li}$	2.03	25.0 meV	45.4 mb	Fraction lost: $\approx 10^{-8}$
${}^7\text{Li}(t,n){}^9\text{Be}$	10.44	2.04	$155 \text{ mb sr}^{-1}$	Fraction lost: $1 \times 10^{-5}$
			Corrections due to ${}^7\text{Li}$ reactions (loss): $0.1 \times 10^{-4}$	
${}^{27}\text{Al}(n,\gamma){}^{28}\text{Al}$		25.0 meV	0.23 b	Measured with PGAA
${}^{28}\text{Al}(\beta){}^{28}\text{Si}$	7.72			Fraction gained: $4 \times 10^{-5}$
				Net loss: $(4.7 \pm 0.4) \times 10^{-4}$

Table 3

List of possible nuclear reactions in the target and the size of the corrections. Only nuclear reactions above threshold for the maximum triton and  $\alpha$  particle energies are listed.

#### 5.4. Neutron Backscattering from the Radiometer Targets

Loss mechanisms for particle beams striking radiometer targets include sputtering, secondary electron emission, and backscattering. For the case of low energy neutrons which penetrate a distance into the absorber that is large compared to the range of the reaction products, the first two mechanisms are negligible [34]. We are left with neutron backscattering.

In order to study and quantify possible power loss due to neutron backscattering, a technique that allows imaging of the backscattered neutrons [35] was developed. The most suitable nucleus for neutron radiography is  ${}^{164}\text{Dy}$  because of its large neutron absorption cross-section (800 b) and the relatively long half-life (138 min) of the activated state which decays by  $\beta$ -emission with a 1.25 MeV endpoint energy. In the measurement, a 50 mm  $\times$  50 mm square of 100  $\mu\text{m}$  thick  ${}^{164}\text{Dy}$  foil was shaped into a half-cylinder and placed in front of the target as depicted in Fig. 8). The setup was placed in an evacuated chamber to suppress air scattering. The beam on the target was tightly collimated by two layers of  ${}^6\text{LiF}$  with a 3.2 mm hole drilled in them. A slightly larger hole was punched into the foil to prevent the direct beam

from irradiating it and creating a hot spot. The foil was thus exposed to, and activated by, the neutrons that were scattered backwards from the target. Measurements were also done in which a piece of foil was exposed to the direct beam, in order to determine the fraction of incident neutrons that are backscattered.

The foil activity was transferred to an image plate where the energy of the  $\beta$ -particles is converted to photo-stimulable-luminescence that can be read by an image reader (a Fujix Model BAS2000 in this case). The image plate response is proportional to the number of  ${}^{165}\text{Dy}$  atoms that decay in the time interval during which the plate is exposed to the activated foil. This imaging process is very sensitive and has a linear response over a dynamic range spanning four decades of intensity.

An image of the backscattered neutrons from the  ${}^6\text{LiMg}$  target is shown in Fig. 9 and results from a couple of measurements are given in table 5.4. The fraction of backscattered neutrons is determined to be  $(0.010 \pm 0.001)\%$  of the incident beam. The reason for the small amount of backscattering is that the energy of the neutrons in the measurement is below the Bragg cutoff for both the  ${}^6\text{LiMg}$  target and the aluminum in the

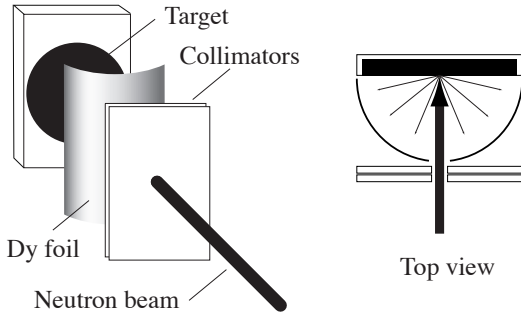


Figure 8. Setup to measure the backscattered neutrons from the radiometer targets.

cover. Thus, there is no Bragg scattering from the crystallites in the solid: only density fluctuations can cause scattering. Furthermore, even the small amount of backscattering we observe in this room temperature measurement, which is due to phonon scattering in the solid, will be smaller at the measurement temperature of 2 K which is far below the Debye temperature of the target. We conclude that neutron backscattering from the target is negligible.

### 5.5. Conductive and Radiative Power Losses from the Radiometer Targets

The power loss from the target by gas conduction is greatly reduced by operating at low temperature. The cold surfaces act as cryopumps, thereby reducing the residual gas pressure, and since the target is the last object to reach low temperature during cooldown it experiences the least gas condensation. Taking helium to be the primary residual gas we estimate the power loss due to gas conduction to be below 0.3 nW, thus below  $10^{-4}$  of the power delivered by the neutrons. In addition, we expect this quantity to be quite stable. The target sees only the inner surface of the 2 K radiation shield, which is in thermal contact with the temperature-controlled heat bath. Thus, the size of the gas conduction power loss remains constant in the beam-on and the beam-off cases and is effectively removed by

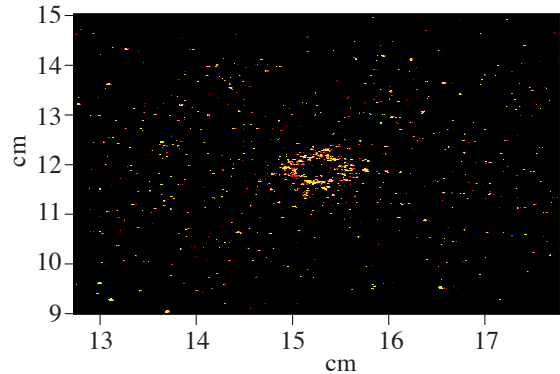


Figure 9. Neutrons backscattered from the  ${}^6\text{LiMg}$  target as recorded on  ${}^{165}\text{Dy}$  foil.

taking the difference. Therefore this power loss mechanism is completely negligible.

The power loss from the target through radiation is given by the Stefan-Boltzmann law. For the case where the emissivities of the surfaces are unity and for target and heat bath temperatures of 2.1 K and 2.0 K respectively, the power transferred by radiation is about 1 nW. Realistic values for emissivity will reduce this estimate by at least an order of magnitude. As in the previous case, the stability of the two temperatures leads to a negligible contribution to the error in the neutron measurement.

There is a slow time-dependence in the feedback power that is required to keep the target temperature constant. The points in Fig. 10 represent the test-input off intervals in the same run as in Fig. 5. Since the runs are started after the daily  $\text{LN}_2$  fill, it is likely that the small extra cooling of the cryostat associated with transient effects of the liquid nitrogen fill gives rise to the change seen in the target feedback power. This transient in the feedback power decays to zero a few hours after the transfer. Note that the time scale of the equilibration is long compared to the 20-minute period of a typical measurement run and its effect is negligible when the difference between input-on and input-off intervals is taken.

File	T <sub>B</sub> (s)	T <sub>T</sub> (s)	T <sub>R</sub> (s)	PSL	N <sub>b</sub>	Backscatter (%)
Scatter 13a	1200	9780	5400	4.9	30.5	0.007
Direct 13a	55	9120	5400	3423.8	20210.5	
Scatter 13b	1200	1440	5400	12.5	39.1	0.009
Direct 13b	60	780	5400	7306.1	21674	

Table 4

Results from the backscattering measurements performed on the  ${}^6\text{LiMg}$  target. The fraction of backscattered neutrons is less than 0.01%.

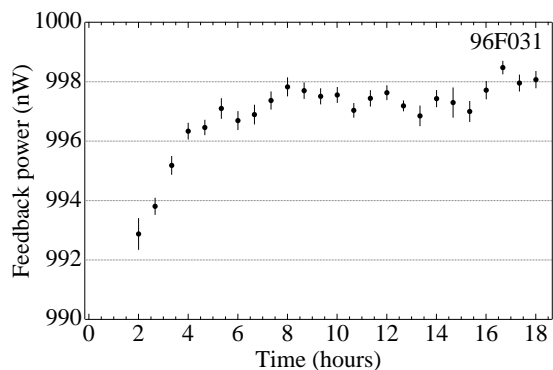


Figure 10. Slow drift in the feedback power that is required to hold the radiometer target temperature constant directly after a transfer of liquid nitrogen into the cryostat. Each point represents an average over 20 minutes.

## 5.6. Neutron Beam Halo

It is clearly essential that the entire neutron beam strike the target and be totally absorbed. By design, we ensured that the neutron beam halo beyond the extent of the target was negligible. To verify this, we measured the neutron intensity distribution just behind the location of the target. Here we briefly describe those aspects of the neutron beamline which are important for assessing possible sources of beam halo and present the beam intensity maps.

A schematic of the beamline is given in Fig. 12. The neutron beam was defined by two  ${}^6\text{LiF}$  apertures. The neutron transmission through this material was measured to be less than  $10^{-4}$ . The beryllium filter between the apertures scatters all neutrons above its Bragg cutoff out of the beam. These neutrons are absorbed in boron-rich shielding around the filter. The beam transmitted through the Be filter is monochromatic and therefore possesses a well-defined maximum divergence set by the collimator geometry and the convolution of the graphite crystal mosaic distribution and the maximum divergence of the neutrons incident on the crystal transmitted by the  ${}^{58}\text{Ni}$  guide.

The rest of the space between the apertures is spanned with a helium gas-filled flight tube to suppress neutron scattering. Helium-4 has a very low scattering cross section ( $\sigma_{scatt} = 0.9$  b). Neutrons scattered in the helium gas are absorbed in boron shielding wrapped around the flight tube and in internal  ${}^6\text{Li}$  plastic beam scrapers.

The solid material seen by the neutron beam after the second collimator is a silicon crystal vac-

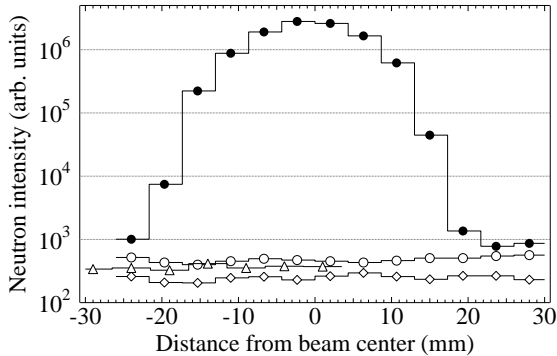


Figure 11. Slices through neutron beam scans at a location immediately behind the radiometer. A 4 mm  ${}^6\text{LiF}$  aperture was affixed to a 4 bar  ${}^3\text{He}$  detector, and the detector-aperture assembly was moved in 4 mm steps. (●) Radiometer out; air gap, (○) radiometer out; air gap; detector plugged, (◇) radiometer in and cold, and (▷) radiometer in, beam shutter closed.

uum window, a silicon crystal target backing in the fluence monitor and the aluminum in the radiation shields. As discussed above the total scattering in the aluminum radiation shields is negligible. The silicon pieces in the beam are both cut from perfect crystals and therefore possess negligible density inhomogeneities that can lead to small angle neutron scattering.

We therefore expect a negligible fraction of neutrons outside the edge of the beam envelope defined by the collimation system and the beam divergence from the crystal. We verified that the beam envelope behaves as expected by performing beam intensity scans at the locations of the fluence monitor and the radiometer target (Fig. 11). The thermal contraction of the cryostat was measured with a theodolite using optical windows on the radiation shields. The target was positioned 3 mm below the beam centerline so that it was aligned when cold.

The absorption of the neutron beam in the target was verified by relative transmission measure-

ments with the target in and out of the beam. The detector was located outside the cryostat and the scanned region was large enough to see any possible halo extending beyond the target. The thickness of the target was chosen to possess a neutron transmission of less than  $10^{-4}$  and the measured transmission was less than  $10^{-4}$ . This verifies that there were no significant inhomogeneities in the target absorption. Based on these measurements we conclude that both the fraction of the beam in a halo which misses the target and the fraction of the neutron beam transmitted through the target are below  $10^{-4}$ .

### 5.7. Energy Stored in Lattice Defects in the Solid Target

The subject of radiation damage in metals has been studied for about five decades, motivated by engineering requirements for fission and fusion energy sources. It is important to have a physical understanding of radiation damage mechanisms in solids to understand why we chose a metallic, low  $Z$  target for the radiometer, why it is difficult to measure experimentally the fraction of energy stored in the target as defects, how the fraction of energy lost to defects is calculated, and why this calculation overestimates the amount of stored energy. These issues are briefly summarized in this section. More details may be found in the extensive literature on the subject [36–39]. It is important to realize at the outset that the fraction of total energy lost in defect creation is typically at the  $10^{-3}$  level in metals.

The  ${}^3\text{H}$  and  ${}^4\text{He}$  reaction products from neutron absorption in  ${}^6\text{Li}$  each carry a few MeV of kinetic energy. These ions lose energy by elastic collisions with the target atoms and inelastic collisions with the target electrons. In metals, the inelastic collisions with electrons either excite core electrons to higher shells or heat the Fermi gas of conduction electrons. For energy loss rates  $\frac{dE}{dx} < 10 \text{ keV nm}^{-1}$ , neither of these processes lead to significant radiation damage because of the rapid redistribution of energy within the electron gas, which then heats the lattice through the electron-phonon interaction. The energy loss rates for  ${}^3\text{H}$  and  ${}^4\text{He}$  slowing down in  ${}^6\text{LiMg}$  are well below this threshold. Secondary photons radiated

upon refilling the bound electron shells possess low enough energy in low  $Z$  materials to be efficiently reabsorbed (this was confirmed in our PIXE and PGAA measurements). For ion velocities higher than the velocities of the electrons, the energy loss process is dominated by a large number of small angle Coulomb scattering events. For the case of ion velocities lower than the electron velocities, the energy loss from atomic scattering increases for a number of reasons. The effective charge of the ion is reduced as it slows down near the end of its range and becomes neutralized. As a result, the Coulomb interaction becomes screened and the atomic collisions more closely resemble hard sphere scattering. Furthermore, the ion velocity falls so far below the velocities of the bound electrons that the electrons move adiabatically in the approaching field of the ion and therefore absorb very little energy from the ion. Some of the atomic collisions displace the atoms from their lattice positions, since in hard sphere scattering all energy transfers up to the maximum kinematically allowed value are equally probable. It is these events, in combination with some smaller fraction (about 10% for MeV ions in metals) of secondary damage from the small fraction of electrons that get high energy transfers, that can cause radiation damage and therefore nonthermal energy storage in the target.

Insulators differ from metals in that a much larger portion of the radiation damage comes from the electronic collisions. The absence of the Fermi gas of conduction electrons means that the thermal diffusivity of the lattice of an insulator is greater than that of its bound electrons and so the electron energy does not dissipate rapidly as in a metal but rather heats the lattice locally. This leads both to extra defect creation by the electrons and to higher defect densities from the more localized energy deposition. Furthermore, insulators support a much broader set of possible defect types and therefore more modes of energy storage than metals. In metals, the dominant form of defect is a vacancy-interstitial pair (a Frenkel defect). In insulators, the prototypical defect is the F-center, which is a negative ion vacancy occupied by an electron. But, in addition, there are other defects with a net local-

ized charge in insulators, each with its own energy. When electron-hole pairs in an insulator are created by energetic electrons, the electrons excited to the conduction band quickly migrate to impurities in the material and modify the charge state of the impurity, while the slow-moving hole is typically self-trapped, forming some positively-charged defect molecule. The interaction of these charged defects is stronger than the attractive interactions between vacancies in metals, leading to defect complexes that are unknown in metals [40]. In some cases, the electron-hole pairs can undergo radiation-less recombination and create more defects. Even ultraviolet light can produce Frenkel defects in alkali halides [41]. For all of these reasons, it is essential to choose a metallic target for the radiometer to minimize possible radiation damage effects.

Technically, the defects are thermodynamically unstable and therefore must relax eventually and produce phonons. However, the relaxation times for lattice defects can be very long, since the relaxation mechanism involves tunneling and/or activation across an energy barrier and is therefore exponentially sensitive to the barrier height. Lattice defects can be mobile in pure metals even at temperatures below 4 K [42–45], but typically this motion is restricted to Stage I recovery, where only a small fraction of the total energy is thermalized. This effect should be suppressed in alloys such as  ${}^6\text{LiMg}$  due to the lower mobility of interstitials and vacancies in a disordered lattice. (Such suppressions have been observed even in dilute alloys [46].) It is difficult to independently measure the amount of energy stored in this form. The dynamics of the process by which defects recombine and eventually release their energy to the lattice are quite complicated, possessing many different relaxation stages as a function of temperature and type of lattice defect, and in some cases one must heat the solid to a within a significant fraction of its melting point before the defects become mobile enough to finally release all of their stored energy to phonons. Given the very small amount of energy that could be stored in the radiometer target in any practical experiment and the difficulty of designing the radiometer to operate as a precision calorimetric device from

Corrections to the radiometer	${}^6\text{LiMg}$ (%)
x- and $\gamma$ - ray production	$\leq 0.001$
Secondary nuclear reactions (calculated)	-0.047 $\pm$ 0.004
Neutron attenuation by windows and target cover	-0.085 $\pm$ 0.01
Neutron backscattering from the target	-0.010 $\pm$ 0.001
Energy stored in lattice defects (calculated)	-0.08 $\pm$ 0.08
Beam halo	$\leq 0.01$
Total radiometer correction	-0.22 $\pm$ 0.09

Table 5

Systematic errors in the radiometer. The fluence loss is expressed as a percentage of the neutron fluence on the target. The total correction is small. The uncertainty in the correction is completely dominated by the uncertainty in the knowledge of the radiation damage energy loss.

cryogenic temperatures to room temperature and beyond, a direct measurement of the fraction of defect formation energy which thermalizes is impractical.

Our approach to the evaluation of this systematic effect is to calculate the fraction of energy that goes into defect formation and to assume that none of this energy is subsequently thermalized by thermal or vacancy-induced diffusion. We use TRIM [47], a Monte Carlo program that simulates the creation of vacancies and interstitials given specific incident ions and target materials. The program [48] draws on the extensive database for H and He ion stopping powers in materials at MeV energies. For compounds such as our binary alloy target, the assumptions involved are described in [49].

The simulation follows each atom in a series of binary collisions whose relative cross sections for electronic and nuclear energy loss are calculated as described in [48]. The inputs to the model are the displacement energy  $E_d$  required to remove an atom from the lattice and place it in an interstitial position, the binding energy of the atom in the solid  $E_b$ , and a cutoff energy  $E_f$  below which the atom is considered to be stopped. In a crystal,  $E_d$  is a strong function of the direction of motion of the atom. Effects dependent on the crystal structure are not included in the TRIM model. Important examples include (1) spatial channeling of the ions along lattice directions, (2) focused collision sequences, which prevent further

multiplication of the damage cascade by generating mainly coherent replacement collisions along a line of atoms and glancing collisions whose energy transfer falls below  $E_d$ , and (3) recombinations of vacancies and interstitials during and just after the cascade. All of these effects reduce the number of displaced atoms and further spread out the spatial distribution of the energy loss [50]. These shortcomings are partially compensated by using a spatially-averaged displacement energy. In addition, TRIM does model an important subclass of replacement collisions in which the incident atom displaces a target atom but is left with less than the displacement energy and falls into the newly created vacancy. This mechanism can reduce the total number of vacancies by 30%.

The minimum and average displacement energies for magnesium are 10 eV and 20 eV respectively [51]. Since there are no reported values in the literature for the displacement energy in lithium, we use the experimentally established correlations of the displacement energy with the sublimation energy  $\Delta H_s$  [52] :

$$E_d = 5\Delta H_s$$

and with the bulk modulus  $B$  and the interatomic distance  $R$  [53]:

$$E_d (\text{eV}) = 0.022B (10^{10} \text{ Pa}) R (10^{-10} \text{ m}) e^{1.18R}$$

to estimate 5 eV to 10 eV for the average displacement energy in lithium. In the TRIM cal-

ulation we took into account the uncertainties in the knowledge of the displacement energy in  ${}^6\text{LiMg}$  by varying the displacement energies by a factor of two. We observed that the variation in the fraction of energy stored in the lattice was much smaller than this factor of two. This is as one would expect, since in the low defect density limit appropriate for our irradiation conditions, fewer defects were formed as the formation energy per defect was increased, so as to keep the total energy in defects approximately constant.

The calculated fraction of the neutron absorption reaction energy for the  ${}^6\text{LiMg}$  target which resulted in defect formation was  $(0.08 \pm 0.01)\%$ . These TRIM simulations also show that loss of energy due to sputtering from the surface is completely negligible. We emphasize that this calculation represents an overestimate of the energy loss due to defects in  ${}^6\text{LiMg}$ . Nevertheless, because this is the only systematic effect in the device which we are unable to measure directly, our approach to the evaluation of this error is as conservative as we can make it: we set the error in the correction to the size of the correction itself. Thus we report the systematic uncertainty due to radiation damage in the target as  $(0.08 \pm 0.08)\%$ .

### 5.8. Summary of Radiometer Corrections

Table 5 lists all of the systematic corrections to the radiometer. The net effect of all the corrections is to reduce the power delivered to the target by the neutron beam by  $(0.22 \pm 0.09)\%$ . The net correction and the sizes of all individual corrections is quite small and on the order of the 0.1% absolute accuracy goal. With all possible loss mechanisms taken into account, we assert that this device measures neutron fluence to 0.08% absolute accuracy.

## 6. Measurements with the Neutron Radiometer

### 6.1. The Experimental Layout

The neutron radiometer was installed on a monochromatic neutron beam at the end of the NG-6 beamline at the NIST Center for Neutron Research. A top-view schematic of the layout is given in Figure 12. The important components

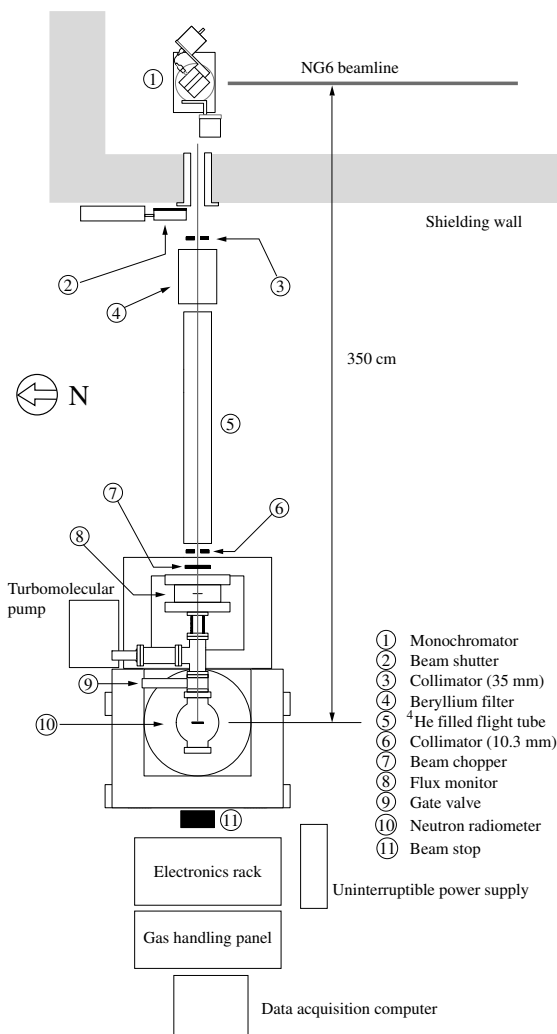


Figure 12. Top view of the layout for the radiometer flux measurement.

of the beamline are as follows:

1. A pyrolytic graphite monochromator that diffracts  $4.963(2)$  Å neutrons out of the main beam.
2. A beryllium filter to reduce the  $\lambda/2$  contamination of the beam. The beryllium crystals are cooled to 77 K to reduce phonon scattering of the  $\lambda$  neutrons.
3.  $^6\text{Li}$ -rich collimators to define the beam.
4. A motorized  $^6\text{LiF}$  chopper. Due to the low  $Z$  of the chopper materials, the chopper has a negligible effect on any  $\gamma$ -rays that might be in the beam and therefore any contribution from  $\gamma$ -disappears to high accuracy in the shutter-on shutter-off difference. Furthermore, the power delivered to the radiometer by possible  $\gamma$ -contamination can be measured by comparing chopper-in data to the main beam shutter-in data. No difference in this power was seen to  $10^{-4}$  accuracy. We conclude any systematic effect from  $\gamma$ -contamination in the beam is completely negligible.
5. A thin fluence monitor which measures the neutron fluence by counting charged particles from the  $n + ^6\text{Li}$  reaction. The fluence monitor rests on a cradle with a kinematic mount and shares a common vacuum with the radiometer.

## 6.2. Response of the Neutron Radiometer to a Chopped Neutron Beam and Analysis of Radiometer Noise

As described earlier, the radiometer measurement involves chopping the neutron beam on and off. Figure 13a shows the incident fluence as a function of time as detected by the fluence monitor located just upstream of the radiometer. The signal from the latter device is shown in Fig. 13b. The typical length for a cycle of 20 minutes is set by the time constant of the radiometer.

The radiometer data is the pair of voltages that are used to calculate the power required to keep the target temperature constant. One of the voltages is that dropped across the heater resistor  $V_H$

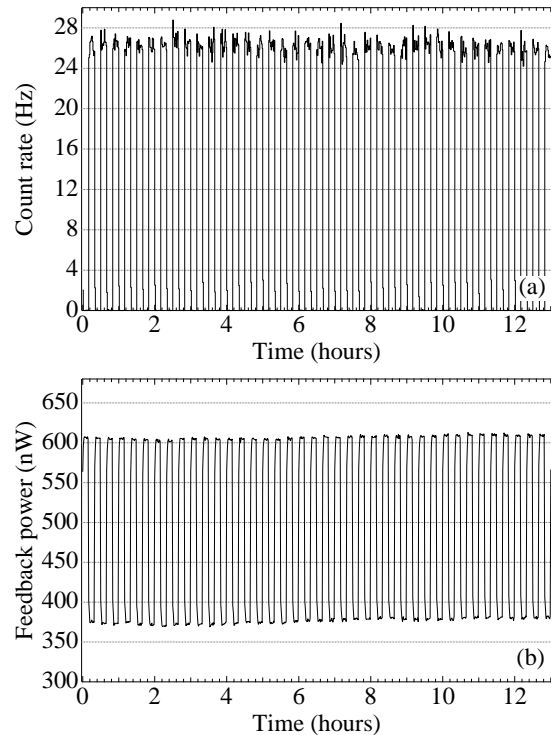


Figure 13. The rate in the fluence monitor and the feedback power for the neutron radiometer as the neutron beam is chopped on and off.

and the other is the voltage  $V_S$  across a shunt resistor  $R_S$ . The last two quantities are used to calculate the current through the heater. The power is

$$P = V_H \frac{V_S}{R_S}. \quad (7)$$

As in the case of the fluence monitor the radiometer data is treated in cycles and the averages are computed for the beam on and beam off intervals. This difference is the power delivered by the neutrons, and the neutron rate is calculated by dividing the power by the Q-value of the reaction. Thus, the conversion factor for the radiometer is simply the inverse of  $(7.66324 \pm 0.00075) \times 10^{-13}$  J.

In the averaging of the half-cycles, not all the points can be used due to the time constant of the radiometer. Discarding the first two points (corresponding to the first two minutes) suffices to avoid transients in the radiometer response. Figure 14 is a plot of the calculated raw (uncorrected for systematic effects) average neutron rate as measured by the radiometer over 20 minute periods.

After the 2 minute transient expected based on the thermal time constant set by the heat capacity and thermal conductance of the weak link, the measured power with neutrons was found to be time-independent. This observation rules out possible systematic effects from the thermal boundary resistance between the  ${}^6\text{LiMg}$  alloy and the aluminum case. If this thermal boundary resistance were too high a long time constant for extracting the neutron-induced power could exist and the neutron power would not be precisely equivalent to the electrical power. We see no evidence for such effects at the  $10^{-4}$  level.

It is important to understand the dominant sources of noise in the radiometer. As with all current-mode devices, the radiometer possesses a noise which is larger than that expected from neutron counting statistics alone due to the extra noise sources that contribute to the power. For neutron radiometry noise sources were analyzed in the linear regime in previous works [5,6] using an equivalent electrical model in frequency space with electrical resistance analogous to thermal resistance, current analogous to power, capacitance

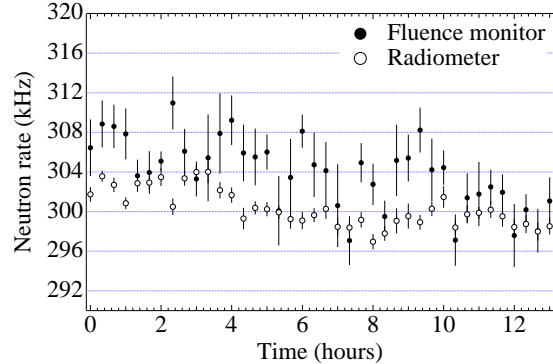


Figure 14. Fluence monitor and radiometer noise compared. Run 99I001 with  ${}^6\text{LiMg}$  radiometer target and Li-930129-H6 fluence monitor target.

analogous to heat capacity, etc. Rather than repeat that analysis, we confine ourselves here to a qualitative discussion.

The two most significant sources of noise in the power measurement beyond neutron shot noise come from noise in the coupling of radiative power into the target and in thermometry noise. (Since the number of phonons created by a neutron absorption is of order  $10^9$ , the extra noise due to fluctuations in the number of secondary quanta produced by neutron absorption is negligible). In our case, we were able to reduce the first noise source to negligible levels by thermally coupling the innermost radiation shield to the heat bath, which is at a temperature very close to that of the target and in addition is thermally stabilized. We are left with thermometry noise. Thermometry noise couples to heat current noise through the target's equivalent impedance,

$$i = \frac{T_n}{Z} \quad (8)$$

which in this case is the parallel combination of the target thermal resistance  $R$  and heat capacity  $C$ :

$$Z = \frac{R}{(1 + j\omega RC)} \quad (9)$$

Thus the heat current noise is frequency-dependent. However, averaged over a bandwidth  $\omega_0 = \frac{2\pi}{\tau}$  where  $\tau$  is the beam-on-beam-off cycle, the noise is

$$(\Delta i)^2 = \int_{\frac{\omega_0}{2}}^{\frac{3\omega_0}{2}} |i|^2 d\omega = \left(\frac{T_n}{R}\right)^2 \left[\omega_0 + \frac{13}{12}\omega_0^3 (RC)^2\right] \quad (10)$$

and for the parameters that characterize our radiometer ( $\omega_0 = 5$  mHz,  $\tau = 90$  sec) the noise is completely dominated by the first (white noise) term, which is about 100 nK Hz<sup>-1/2</sup> for our thermometry. This is larger than the neutron shot noise by a factor of two. Since the fluence monitor absorbs about 1% of the beam and possesses noise completely dominated by neutron counting statistics, we expect the noise in the radiometer to be lower than the noise in the fluence monitor by about a factor of 5, which is what is observed in the data.

## 7. Conclusion

The neutron radiometer described in this work has been demonstrated to be capable of measuring neutron fluences of 10<sup>5</sup> n/s to an absolute accuracy of 0.1%. It can therefore be used to calibrate the efficiency of the fluence monitor used in the neutron lifetime experiment at NIST to 0.1% absolute accuracy on a monochromatic beam. Finally this efficiency will be used in the Penning trap neutron lifetime experiment to determine the neutron lifetime.

All of the systematic corrections to the power measured by the radiometer are at or below 0.1%. All but two of these corrections are measured. The correction due to induced nuclear reactions is small and the nuclear reactions which contribute to it are well-measured. The correction for radiation damage is the largest correction in size (0.08%) and in its uncertainty. The radiation damage correction can be evaluated indirectly if one uses a liquid target which will be free of such radiation damage effects. As mentioned in the introduction, <sup>3</sup>He is the only possibility. The greatest disadvantage of the <sup>3</sup>He is that the Q-value of the neutron absorption reaction is less than one-sixth of the <sup>6</sup>Li reaction and the heat capacity per unit neutron attenuation length is

larger than for the lithium target. The data runs will have to be longer than those with the <sup>6</sup>Li target to attain the required statistical precision. Construction of a radiometer based on <sup>3</sup>He is in progress.

We would like to acknowledge J. David Robertson of the Nuclear and Radioanalytical Chemistry Department at the University of Kentucky for help with the PIXE measurements, Dick Lindstrom of NIST/Gaithersburg for help with the PGAA measurements performed on NG7 at the NIST Cold Neutron Research Facility, Michael Mitch of NIST for help with the operation of the neutron image plate reader for the neutron backscattering measurements, and J. Ziegler of IBM for a copy of the TRIM program. W. M. Snow thanks the Institute for Nuclear Theory at the University of Washington for its hospitality and the Department of Energy for partial support during the completion of this work.

## REFERENCES

1. H. Abele, Nucl. Instrum. Methods **A440**, 499 (2000).
2. R. E. Lopez and M. S. Turner, Phys. Rev. D **59**, 103502 (1999).
3. J. Byrne, P. G. Dawber, J. A. Spain, A. P. Williams, M. S. Dewey, D. M. Gilliam, G. L. Greene, G. P. Lamaze, R. D. Scott, J. Pauwels, R. Eykens and A. Lamberty, Phys. Rev. Lett. **65**, 289 (1990).
4. D. M. Gilliam, G. L. Greene, and G. P. Lamaze, Nucl. Instrum. Methods **A284**, 220 (1989).
5. R. G. H. Robertson and P. E. Koehler, Nucl. Instrum. Methods **A251**, 307 (1986).
6. J. M. Richardson, T. E. Chupp, R. G. H. Robertson and J. F. Wilkerson, Nucl. Instrum. Methods **A306**, 291 (1991).
7. J. M. Richardson, Ph.D. thesis, Harvard University, 1993.
8. J. M. Richardson, W. M. Snow, Z. Chowdhuri, and G. L. Greene, IEEE Trans. Nuc. Sci. **45**, 550 (1998).
9. H. H. Andersen, *A Low-Temperature Technique for Measurement of Heavy Particle*

- Stopping Powers of Metals*, Risø Report No. 93, 1965.
10. H. H. Andersen, C. C. Hanke, H. Sorenson, and P. Vajda, *Phys. Rev.* **153**, 338 (1967).
  11. C. A. van de Runstraat, R. Wijnaendts van Resandt, and J. Los, *J. Phys. E* **3**, 575-578 (1970).
  12. S. R. Gunn, *Nucl. Instrum. Methods* **135**, 251-256 (1976).
  13. F. Hengstberger, *Metrologia* **13**, 69-78 (1977).
  14. H. Burckhart, R. Diehl, and B. Ziegler, *Nucl. Instrum. Methods* **159**, 1-6 (1979).
  15. J. Schivell, G. Renda, J. Lowrance, and H. Hsuan, *Rev. Sci. Instrum.* **53**, 1527-1534 (1982).
  16. T. J. Quinn and J. E. Martin, *Philos. Trans. R. Soc. London* **316**, 6 (1985).
  17. F. Hengstberger, ed. *Absolute Radiometry: Electrically Calibrated Thermal Detectors of Optical Radiation* (Academic Press, 1989).
  18. V. P. Ershov, V. V. Fimuskin, M. V. Kulikov, Yu. K. Pilipenko, and V. B. Shutov, *Nucl. Instrum. Methods* **A385**, 435-437 (1997).
  19. H. Rabus, V. Persch, and G. Ulm, *Appl. Opt.* **36**, 5421 (1997).
  20. C. D. Reintsema, J. A. Koch, E. N. Grossman, *Rev. Sci. Instrum.* **69**, 152-163 (1997).
  21. A. C. Parr, *A National Measurement System for Radiometry, Photometry, and Pyrometry Based Upon Absolute Detectors*. NIST Technical Note 1421 (1991).
  22. C. S. Barrett, *Acta Crystallog.* **9**, 671 (1956).
  23. A. W. Overhauser, *Phys. Rev. Lett.* **53**, 64 (1984).
  24. R. Berliner and S. Werner, *Physica* **136B**, 481 (1986).
  25. R. Berliner and S. Werner, *Phys. Rev.* **B34**, 33 (1986).
  26. R. Berliner, O. Fazen, H. G. Smith, and R. L. Hitterman, *Phys. Rev.* **B40**, 12086 (1989).
  27. W. Schwarz and O. Blaschko, *Phys. Rev. Lett.* **58**, 1228 (1987).
  28. M. Goswami, F. Ahmed, and L. S. Kothari, *Ann. Nucl. Energy* **17**, 549 (1990).
  29. M. Goswami and F. Ahmed, *Ann. Nucl. Energy* **25**, 1 (1998).
  30. T. B. Massalski, ed., *Binary Alloy Phase Diagrams*, 2nd ed. (ASM International, 1990).
  31. W. R. Lozowski, *Nucl. Instrum. Methods* **A397**, 46 (1997).
  32. J. G. Ziegler and N. B. Nichols. *ASME Trans.* **64**, 759 (1942).
  33. **ZHANG 93 FIND THIS**
  34. G. M. McCracken, *Rep. Prog. Phys.* **38**, 241 (1975).
  35. Y. T. Cheng, T. Soodprasert and J. M. R. Hutchinson, *Appl. Radiat. Isot.* **47**, 1023 (1996).
  36. E. Friedland, *Crit. Rev. Solid State* **26**, 2 (2001).
  37. M. Nastasi, J. W. Mayer and J. K. Hirvonen, *Ion-Solid Interactions: Fundamentals and Applications* (Cambridge University Press, 1996).
  38. L. T. Chadderton and I. M. Torrens, *Fission Damage in Crystals* (Methuen & Co Ltd., 1969).
  39. H. Ullmaier, ed., *Atomic Defects in Metals* Landolt-Bornstein, New Series Group III, Vol. 25 (1991).
  40. J. H. Crawford and L. M. Slifkin, eds., *Point Defects in Solids* (Plenum Press, 1972).
  41. A. Goland, in *Radiation Damage in Metals*, ed. N. L. Peterson and S. D. Harkness, American Society for Metals, p. 366 (1976).
  42. R. R. Coltman, C. E. Klabunde, J. K. Redman, and J. M. Williams, *Radiat. Eff.* **24**, 69 (1975).
  43. P. S. Gwozdz and J. S. Koehler, *Phys. Rev.* **B8**, 3616 (1973).
  44. J. Fuss and H. Schultz, *Radiat. Eff.* **40**, 181 (1979).
  45. H. Schroeder and W. Schilling, *Radiat. Eff.* **30**, 243 (1976).
  46. C. P. Cannon and A. Sosin, *Radiat. Eff.* **25**, 253 (1975).
  47. J. F. Ziegler, TRIM: *TRansport of Ions in Matter* program documentation, 1994.
  48. J. F. Ziegler, *The Stopping and Range of Ions in Solids* (1985).
  49. J. F. Ziegler and J. M. Manoyan, *Nucl. Instrum. Methods* **B35**, 215 (1989).
  50. M. W. Thompson, *Defects and Radiation Damage in Metals* (Cambridge University Press, 1969).
  51. H. H. Andersen, *Appl. Phys.* **18**, 131 (1979).

52. T. E. Mitchell, *Fundamental Aspects of Radiation Damage in Metals*, eds. M. T. Robinson and F. W. Young, US GPO, Washington, DC, vol. 1, p. 76 (1976).
53. P. Jung, *Radiat. Eff.* **35**, 155 (1978).